


## Polarization Interference and Modulation in the Low-Frequency Range

Shi-qian Zhang,<sup>1</sup> Jie-ying Ma,<sup>1</sup> Yong Zhang,<sup>1</sup> Ling-bao Kong,<sup>2</sup> and Cheng-ping Huang<sup>1,\*</sup>

<sup>1</sup>*Department of Physics, Nanjing Tech University, Nanjing 211816, China*

<sup>2</sup>*Department of Physics, Beijing Technology and Business University, Beijing 100048, China*

 (Received 26 September 2021; accepted 30 November 2021; published 17 December 2021)

Conventional polarized light interference is realized by using the natural crystals sandwiched between two linear polarizers, which has applications in optical signal modulation and photomechanics. However, due to a shortage of suitable birefringent materials, a similar effect has not been reported in the low-frequency range. In this paper, a compact and tunable polarization interference system working in the microwave band has been proposed, employing artificially structured planar materials, i.e., two metal screens perforated with subwavelength apertures. One screen splits the incident linear polarization into two orthogonal electric components and the other combines the parallel electric components (in a certain direction) to induce an interference. We find that the near-field coupling between the two metal screens plays a crucial role and the polarization interference effect is strongly dependent on the lateral dislocation of the system. The theory and experiment demonstrated that, by laterally displacing one metal screen (at the millimeter scale), a nearly linear modulation of transmission intensity (93.1%–1.4%) can be achieved. The proposed effect can be extended to the THz range and may be valuable for constructing the microwave or THz modulators.

DOI: [10.1103/PhysRevApplied.16.064046](https://doi.org/10.1103/PhysRevApplied.16.064046)

### I. INTRODUCTION

Interference of polarized light, typically employing a birefringent wave plate sandwiched between two linear polarizers (or similar optical systems), is well known and widely used in optics [1–3]. Due to the birefringence effect, the incident light is decomposed into ordinary and extraordinary waves and a phase difference, which is proportional to the product between refractive-index difference of the two waves and thickness of the wave plate, can be induced. Depending on the value of phase difference (odd or even times of  $\pi$ ), destructive or constructive interferences of light is thus achieved. Moreover, by using the electro-optic, magneto-optic, or elastic-optic effects [1,4,5], the material refractive index and birefringence can be controlled with the external electric field, magnetic field, or stress. This leads to wide applications in constructing the optical modulators, switches, filters and sensors, etc. [6–12]. Nonetheless, because of the weak birefringence effect of natural crystals or small index variation induced externally, the wave plate is usually bulky (with the thickness much larger than the working wavelength), which is not conducive to the integration and active control of optical devices. This issue becomes much more prominent when the frequency extends from optical to THz or microwave regime, due to

the larger working wavelength and the shortage of suitable natural birefringent materials. Although anisotropy may be introduced in the THz or microwave region by designing metamaterials [13–16], an active and efficient control of the birefringence effect is still difficult. Therefore, the generation and dynamic control of polarization interference with compact devices become challenging in the low-frequency region.

In this paper, we propose a scheme to extend the polarization interference effect from the optical to microwave band. For this propose, artificially structured planar materials, i.e., two closely spaced perforated metal screens are employed. The first metal screen is milled with pairs of perpendicular rectangular holes, where the incident wave is divided into two orthogonal electric components. The two orthogonal components can be coupled into the second metal screen that is patterned with vertical rectangular holes, giving rise to the polarization interference effect. It is stressed that the near-field coupling between the two metal screens plays a crucial role, which dominates both the amplitude and phase of the interfering electric components (in contrast, the phase difference of the birefringent crystals is governed by the crystal length and the birefringence effect). Accordingly, the thickness of system is one order of magnitude smaller than the working wavelength. Moreover, by laterally translating the second metal screen, the near-field coupling of the screens and polarization interference effect can be dynamically modulated. The

\*cphuang@njtech.edu.cn

theory and experiment demonstrated that a nearly linear variation of transmission intensity (from 93.1% to 1.4%) with the lateral displacement of metal screen (of millimeter scale) can be realized. The effect can be extended to the THz regime and is useful for designing the microwave or THz modulators, switches, etc.

## II. WORKING MECHANISM

Figure 1 shows the schematic view of the polarization interference system (here only one unit cell is shown), which is composed of two parallel metal screens (I and II) milled with periodic subwavelength apertures. Metal screen I is perforated with the hole dimers consisting of two perpendicular rectangular holes (holes *A* and *B*), and the metal screen II is perforated with vertical rectangular holes (hole *C*). Here, the thickness of the two metal screens is *t*, the spacing of the two screens is *g*, the lattice period of the rectangular holes and hole dimers is *p*, and the length and width of all rectangular holes is *l* and *w*, respectively (the separation between the two dimer holes in screen I is *a*). To tune the system efficiently, hole *C* in screen II is displaced by *s* with respect to the vertical central line of the unit cell (this lateral displacement can be realized by mechanically translating the whole metal screen II along the *x* axis). A linearly polarized wave, with the polarization angle  $\theta$  (with respect to the *y* axis), propagates along the  $-z$  axis and incidents normally upon metal screen I. The transmission of waves is generated through metal screen II with the *x* polarization. Note that, although a polarization rotation (with the magnitude of  $90^\circ - \theta$ ) is involved here, our interest is concentrated on the polarization interference

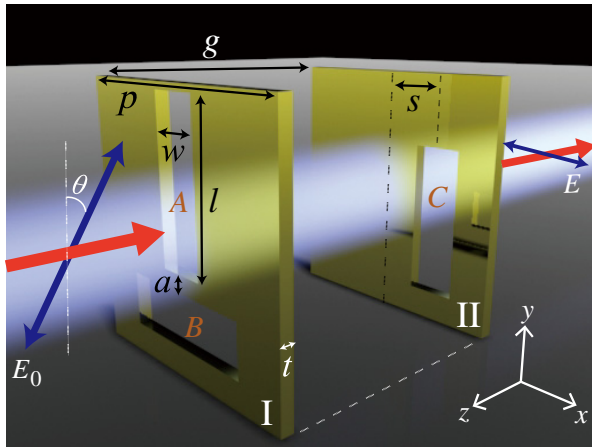


FIG. 1. Schematic view of unit cell of the tunable polarization interference system, which is composed of two perforated and closely spaced metal screens. The linearly polarized wave, with a polarization angle  $\theta = 45^\circ$ , propagates along the  $-z$  axis and incidents normally upon metal screen I. By translating metal screen II in the *x* direction, the tuning of polarization interference effect can be achieved.

(by superposition of two parallel components) instead of the polarization conversion (usually by superposition of two orthogonal components). The latter has also been studied employing the double-layer subwavelength structures [17–19].

The main idea of this work is as follows. When the incident wave impinges on metal screen I, the inclined incident polarization can be decomposed into *x* and *y* components, which excite the vertical hole *A* and horizontal hole *B*, respectively. In this case, metal screen I behaves somewhat like a sheet of birefringence crystal (if screen II is absent, two transmitted orthogonal polarization states will be produced; in principle, the phase difference may be introduced by using the holes of different sizes). When metal screen II is placed parallel and closely to screen I ( $g \ll \lambda$ ), the two orthogonal electric components induced in holes *A* and *B* will couple, respectively, with the vertical hole *C* in screen II, thus giving rise to the *x*-polarized transmission. Here, metal screen II functions as a coupler and linear polarizer (the polarization is along the short edges of the rectangular holes; the transmission of electric component along the long hole edges will be cut off). Because of the simultaneous coupling between holes *A* and *C* and between holes *B* and *C*, a polarization interference effect in both the near-field and far-field regions can be expected. Moreover, as shown in Sec. III, the coupling between holes *A/B* and *C* is strongly dependent on the lateral displacement *s*. Thus, by translating metal screen II, the polarization interference effect may be modulated dynamically.

The above mechanism can be better understood with the help of a semianalytical model. For incident wave with inclined polarization, the total transmission response of the system will be dominated by the superposition principle. That is, the complex transmission amplitude (with the *x* polarization) is the sum of the individual amplitudes (which are also *x* polarized) that would have been separately induced by the two orthogonal electric components of the incident field [20]:

$$\varepsilon_{Tx} = E_0 \sin \theta t_{xx} e^{i\varphi_{xx}} + E_0 \cos \theta t_{xy} e^{i\varphi_{xy}}. \quad (1)$$

Here,  $E_0$  is the incident electric field,  $t_{ij}$  (the subscript  $i = x$  represents the transmitted field with *x* polarization,  $j = x$  or *y* represents the incident field with *x* or *y* polarization) is the real transmission coefficient of electric field, and  $\varphi_{ij}$  is the corresponding field transmission phase.

To enhance the polarization interference effect, we consider the case that  $E_0$  is inclined with a polarization angle of  $\theta = 45^\circ$ . Accordingly, the power transmission efficiency  $T = |\varepsilon_{Tx}/E_0|^2$  can be determined as

$$T = \frac{t_{xx}^2 + t_{xy}^2}{2} + t_{xx} t_{xy} \cos \delta. \quad (2)$$

Here,  $\delta = \varphi_{xy} - \varphi_{xx}$  is the transmission phase difference between the  $x$ - and  $y$ -polarized incident waves; the second term on the right-hand side of Eq. (2) represents the interfering contribution. Hence, a polarization interference effect in the far field can be achieved. When the phase difference  $\delta = 0$  and  $\pi$ , Eq. (2) gives the transmission maximum  $T_{\max} = (t_{xx} + t_{xy})^2/2$  and minimum  $T_{\min} = (t_{xx} - t_{xy})^2/2$ , respectively. If the transmission coefficients satisfy  $t_{xx} = t_{xy}$ , the transmission maximum and minimum can be further simplified as  $T_{\max} = 2t_{xx}^2$  and  $T_{\min} = 0$ . Therefore, if the transmission phases and amplitudes can be manipulated, an efficient tuning of the polarization interference effect may be realized.

Although the effect is similar to the conventional polarized light interference, the differences between them are significant. On the one hand, the separation of two metal screens in our system will be one order of magnitude smaller than the wavelength, thus the coupling is mainly bridged by the evanescent fields. In contrast, the propagating waves are employed in a conventional system and the thickness of birefringent crystal is much larger than the wavelength. On the other hand, the amplitudes and phase difference of the two interfering electric components in our system are governed and efficiently controlled by the lateral displacement of metal screen. But the phase difference in the conventional system originates from and is severely constrained by the minor birefringence effect of the natural crystals. Our system is compact, designable, and freely tunable. The unique characteristics of the artificial system enable us to extend the polarization interference effect to the low-frequency region.

### III. RESULTS AND DISCUSSIONS

We focus on the microwave band (with the frequency 3.0–4.5 GHz or wavelength 66–100 mm) and the structural parameters of the perforated metal (aluminum) screens are set as follows. The thickness of two free-standing metal screens is  $t = 1.5$  mm, the lattice period of hole array is  $p = 60$  mm, the length and width of all rectangular holes are  $l = 40$  mm and  $w = 10$  mm, respectively (the separation of dimer holes in screen I is  $a = 6$  mm). To ensure an efficient near-field coupling, the spacing of the two metal screens is set as  $g = 10$  mm, which is much smaller than the working wavelength (approximately 83 mm). As the structural sizes are subwavelength ( $p < \lambda$ ), only the zero-order modes of the system are propagating (which lead to the zero-order transmission and reflection); the higher-order diffraction modes are evanescent and bounded near the metal surfaces (which will contribute to the near-field coupling between the two metal screens). In addition, to theoretically study the effect, numerical simulations based on the finite-difference time-domain (FDTD) method have been carried out for our system. In the simulation, periodic boundary conditions in the  $x$ - $y$  plane and open boundary

condition in the  $z$  direction are employed. The dispersion of aluminum screens is described by  $\varepsilon_m = 1 + i\sigma/\varepsilon_0\omega$ , where the metal conductivity is  $\sigma = 3.5 \times 10^7$  S/m.

It is found that the near-field coupling between the two perforated metal screens is strongly dependent on the screen's lateral displacement  $s$  [21]. This  $s$  dependence may be used here to control the transmission coefficients  $t_{ij}$  and phase difference  $\delta$ . To study this point, Figs. 2(a) and 2(b) present the simulated spectra of  $t_{ij}$  and  $\delta$ , taking the lateral displacement  $s = \pm 6$  mm as an example. For the transmission coefficient  $t_{xx}$  or  $t_{xy}$  [Fig. 2(a)], the spectra are identical for positive and negative displacement  $s$  [ $t_{ij}(-s) = t_{ij}(s)$ ]. Also, both  $t_{xx}$  and  $t_{xy}$  exhibit an outstanding peak in the spectra near the frequency 3.63 GHz (the peak position is close to the cutoff frequency, 3.75 GHz, of the single rectangular holes and thus can be attributed mainly to the hole waveguide resonance; the peak positions deviate slightly from each other, due to the coupling of different rectangular holes). The peaks of  $t_{xx}$  and  $t_{xy}$  own comparable amplitudes, which indicate that both  $x$  and  $y$  component of incident wave can pass through the coupled metal screens (via the holes  $A$ - $C$  coupling and  $B$ - $C$  coupling, respectively).

Figure 2(b) shows that the phase difference  $\delta$  is very close to 0 or  $\pi$  in the considered wavelength region (when the incident wave is changed from  $x$  to  $y$  polarization, the phase of waveguide mode of hole  $C$  will be either maintained or reversed, depending on the sign of  $s$ ). This is associated with the near-field interactions of surface charges accumulated near the long edges of rectangular holes [21]. Moreover, the phase difference  $\delta$  has a  $\pi$  shift for the opposite sign of  $s$ :  $\delta(-s) = \delta(s) + \pi$ . This

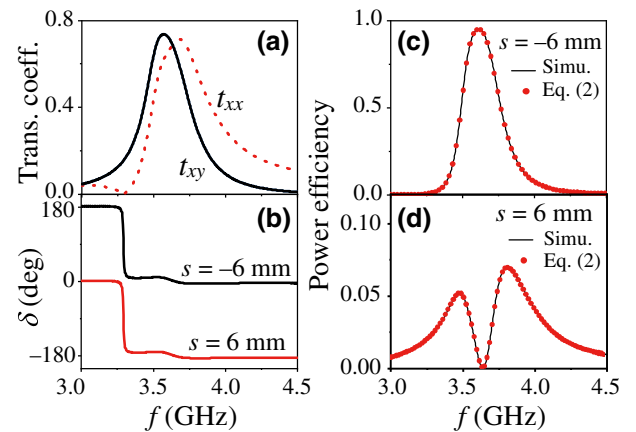


FIG. 2. (a) Field transmission coefficients ( $t_{xx}$  and  $t_{xy}$ ) and (b) difference of transmission phase ( $\delta = \varphi_{xy} - \varphi_{xx}$ ) as a function of frequency, for  $x$ - and  $y$ -polarized incident wave (the lateral displacement is  $s = \pm 6$  mm). (c), (d) The calculated power transmission efficiency for  $45^\circ$ -polarized incident wave, where  $s$  is  $-6$  mm (c) and  $6$  mm (d) [the line and circles represent the results of simulation and Eq. (2), respectively].

means, when screen II is displaced from  $s = -6$  mm to  $s = 6$  mm, the two parts of transmission contributed by the  $x$  and  $y$  components of incident wave will vary from in phase to antiphase. They correspond to the constructive and destructive polarization interferences, respectively.

To confirm the above point, Figs. 2(c) and 2(d) present the simulated zero-order transmission spectra (the solid lines) for  $45^\circ$ -polarized incident wave, where the lateral displacement is  $-6$  and  $6$  mm, respectively. When  $s = -6$  mm, as shown in Fig. 2(c), a prominent transmission peak appears at the frequency  $3.63$  GHz with the efficiency reaching  $94.6\%$ . However, when  $s = 6$  mm, as shown in Fig. 2(d), the transmission efficiency of the system is greatly suppressed, with the efficiency less than  $7\%$  from  $3$  to  $4.5$  GHz and near zero around  $3.63$  GHz. Moreover, the power transmission efficiency is calculated using Eq. (2) (where  $t_{xx}$ ,  $t_{yy}$ , and  $\delta$  are given by the numerical values). The results are also shown in Figs. 2(c) and 2(d) by the solid circles. As expected, the curves from the numerical simulations (the solid lines) coincide completely with the semianalytical ones, showing that the system is indeed governed by the polarization interference effect. The above results also suggest that a displacement of metal screen can switch the system from constructive to destructive interference and lead to a significant variation of transmission efficiency.

Figure 3 presents the amplitude distributions of electric field in screens I and II in the case of  $s = -6$  mm [(a) and (b)] and  $s = 6$  mm [(c) and (d)], where the working frequency is  $3.63$  GHz. One can see that, due to

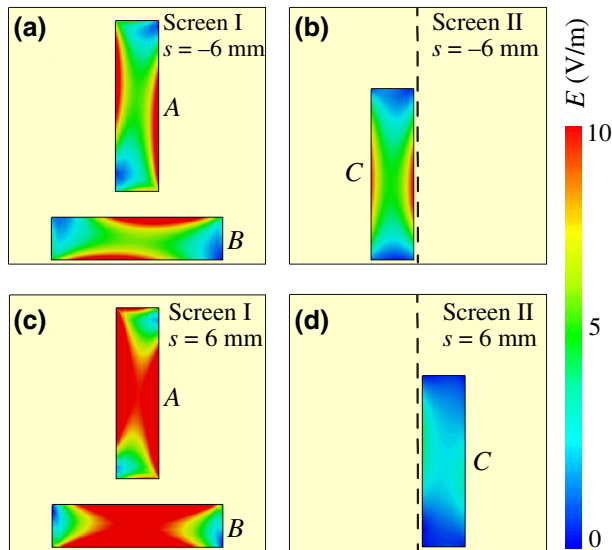


FIG. 3. Amplitude distributions of electric field for metal screens I and II: (a),(b)  $s = -6$  mm and (c),(d)  $s = 6$  mm (the operating frequency is  $3.63$  GHz). The wave is normally incident on the sample with the electric field of  $1$  V/m and polarization angle of  $45^\circ$ .

the inclined polarization of incident wave, the rectangular holes  $A$  and  $B$  in screen I can be strongly excited in both cases. However, the waveguide mode in the rectangular hole  $C$  of screen II shows a significant difference: the hole electric field is strong for  $s = -6$  mm (b) and weak for  $s = 6$  mm (d) (the field monitored by a probe placed  $0.1$  mm away from the hole exit is even close to  $0$ ; not shown here), consistent with the transmission features observed in Fig. 2. This means a constructive or destructive interference effect also exists in the near-field region (i.e., in hole  $C$ ), associated with the near-field coupling between holes  $A/B$  and  $C$  as well as the superposition of electric field in hole  $C$ . The electric field in hole  $C$  is proportional to the electric dipole moment induced around hole  $C$  and thus proportional to the far-field radiation of the system. It is worth noting that, compared with  $s = -6$  mm (a), the fields in holes  $A/B$  are much stronger for  $s = 6$  mm (c). In the latter case, more electromagnetic energy is concentrated temporarily in holes  $A$  and  $B$ ; the concentrated energy will be released ultimately via the zero-order reflection (approximately  $98\%$ ), as the transmission channel is blocked (the simulation shows that the absorption of metal, which is usually weak in the low-frequency range, is only about  $2\%$ ).

The relationship between the field-transmission coefficients and phase difference and lateral displacement  $s$  is simulated [see Figs. 4(a) and 4(b)], where the working frequency is fixed as  $3.63$  GHz. One can see from Fig. 4(a) that, when  $s$  varies from  $0$  to  $\pm 8$  mm,  $t_{xx}$  decreases gradually from  $1$  to  $0.25$  and  $t_{yy}$  increases almost linearly from  $0$  to  $0.92$ . Thus there is a trade-off between the coupling of holes  $A-C$  and the coupling of holes  $B-C$ : with the increase

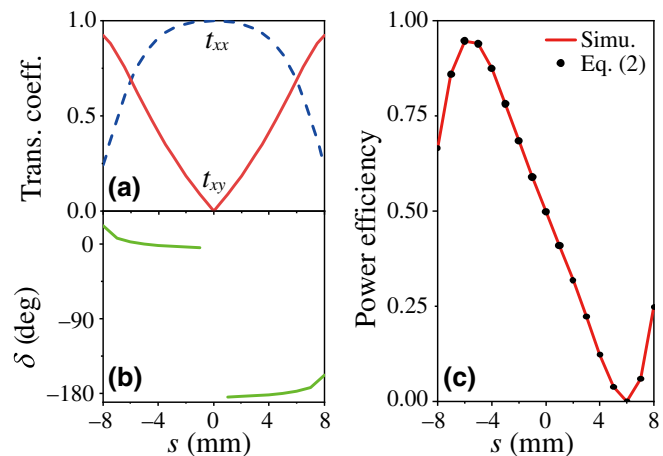


FIG. 4. (a) Field transmission coefficients and (b) phase difference  $\delta$  as a function of lateral displacement  $s$ . (c) Power transmission efficiency as a function of  $s$  for  $45^\circ$ -polarized incident wave [the line and circles are obtained from simulation and Eq. (2), respectively]. Here, the working frequency is fixed as  $3.63$  GHz.



of  $s$ , the near-field coupling between the parallel rectangular holes  $A$  and  $C$  becomes weaker, whereas the coupling between the perpendicular holes  $B$  and  $C$  gets stronger. Consequently, the amplitude of transmission coefficients can be efficiently controlled. Figure 4(b) shows that the phase difference  $\delta$  is not very sensitive to the lateral displacement  $s$ , except that  $\delta$  is close to  $0^\circ$  when  $s$  varies from  $-8$  to  $0$  mm and close to  $-180^\circ$  when  $s$  varies from  $0$  to  $8$  mm. Therefore, the polarization interference is constructive when  $s < 0$  and destructive when  $s > 0$ . Combining the above two points, a continuous and efficient modulation of polarization interference effect can be achieved. Figure 4(c) presents the simulated power transmission efficiency (the solid line) as a function of  $s$  ( $f = 3.63$  GHz). The result predicted by Eq. (2) is also plotted in Fig. 4(c) (the solid circles), showing a good agreement. Indeed, the power efficiency is strongly dependent on the lateral displacement. Particularly, when  $s$  varies from  $-6$  to  $6$  mm, the transmission efficiency decreases almost linearly from  $94.6\%$  to  $0.0\%$  (note that when  $s = \pm 6$  mm,  $t_{xx} = t_{yy}$ , leading to the transmission maximum and minimum). The result is useful for constructing the compact microwave modulators.

Based on the above theoretical results, experimental demonstration of the effect is carried out. In the experiment, the perforated metal (aluminum) screens are fabricated with the laser-cutting method. The hole array of the screens consists of  $10 \times 10$  units, with the screen's side length (approximately  $600$  mm) much larger than the wavelength. Figures 5(a) (screen I) and 5(b) (screen II) present the photographs of parts of the two perforated metal screens. To realize the lateral displacement, the two metal screens are placed on and controlled with a two-dimensional mobile mechanical platform (the accuracy of displacement is  $0.1$  mm). Two rectangular horn antennas, serving as the emitter and receiver of the linearly polarized microwave (the polarization of wave emitted by the antenna is along the short edges of the rectangular horn), are placed in front of and behind the two metal screens, respectively (the separation between the two horn antennas is  $2$  m). The transmission spectrum at normal incidence is recorded by the vector network analyzer (The 41st Research Institute of China Electronics Technology Group Corporation, AV3629A).

By varying the lateral displacement  $s$  carefully, the transmission spectra of the system have been obtained experimentally (the incident wave is  $45^\circ$  polarized). Figure 5(c) presents the measured transmission spectra (symbols), where the lateral displacement  $s$  is set as  $-6$ ,  $-3$ ,  $0$ ,  $3$ , and  $6$  mm, respectively. For comparison, the simulated spectra are also mapped in Fig. 5(c) by the solid lines. One can see that the experimental and simulated results are in good agreement with each other (some deviations can be attributed to the experimental errors). The measurement confirms that a transmission peak appears

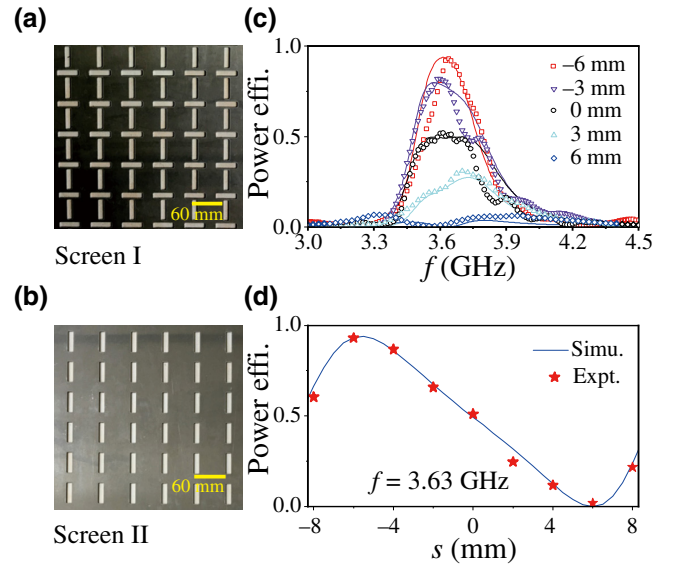


FIG. 5. (a),(b) Partial photographs of two metal screens milled with subwavelength apertures: (a) perpendicular rectangular hole dimers (screen I); (b) vertical rectangular holes (screen II). (c) Measured (symbols) and simulated (lines) power transmission efficiency as a function of frequency ( $s$  is  $-6$ ,  $-3$ ,  $0$ ,  $3$ , and  $6$  mm, respectively). (d) Measured (symbols) and simulated (line) power efficiency as a function of lateral displacement  $s$  ( $f = 3.63$  GHz). Here, the incident wave is  $45^\circ$  polarized.

around  $3.6$  GHz and that, with the variation of  $s$ , the transmission efficiency decreases considerably. At the frequency of  $3.63$  GHz, the measured maximal transmission efficiency is  $93.1\%$  for  $s = -6$  mm and the measured minimal efficiency is  $1.4\%$  for  $s = 6$  mm. Figure 5(d) presents the measured (symbols) and simulated (line) power transmission efficiency as a function of lateral displacement  $s$  ( $f = 3.63$  GHz). Again, a good agreement between the theory and experiment can be seen. Moreover, a nearly linear relationship between the measured power efficiency and lateral displacement ( $s = -6$ – $6$  mm) is clearly manifested.

In the above study, we focus on the polarization interference and modulation for a specific polarization angle, i.e.,  $\theta = 45^\circ$ . If the incident polarization is rotated with an arbitrary polarization angle  $\theta$ , Eq. (2) is modified as

$$T = t_{xx}^2 \sin^2 \theta + t_{yy}^2 \cos^2 \theta + t_{xx} t_{yy} \sin 2\theta \cos \delta. \quad (3)$$

Because of the dependence of transmission coefficients ( $t_{xx}$  and  $t_{yy}$ ) and phase difference  $\delta$  on the lateral displacement  $s$ , a modulation may also be achieved for an arbitrary  $\theta$ . Based on Eq. (3) and numerical values in Figs. 4(a) and 4(b), the power transmission efficiency as a function of the polarization angle and lateral displacement is calculated ( $f = 3.63$  GHz) and the results are shown in Fig. 6. We can see that an obvious transmission modulation with the variation of  $s$  is present in a wide range of  $\theta$  [from  $0^\circ$  to

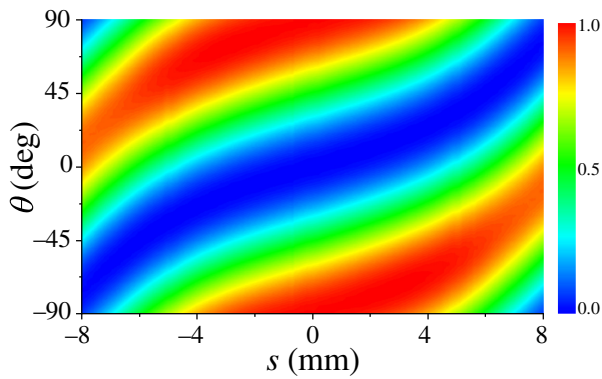


FIG. 6. Power transmission efficiency as a function of the polarization angle  $\theta$  and lateral displacement  $s$  [calculated with Eq. (3)]. The structural parameters are the same as those used previously and the working frequency is set as 3.63 GHz.

$\pm 90^\circ$ , where  $T(\theta, s) = T(-\theta, -s)$ . But the detailed modulation behavior depends on the angle  $\theta$ , where  $\theta = \pm 45^\circ$  corresponds to a maximal interfering term in Eq. (3) and to a typical and efficient modulation effect. It is also noted that, although the polarization interference occurs in most cases, two special situations should be excluded here. When  $\theta = 0^\circ$  ( $T = t_{xy}^2$ ) or  $\pm 90^\circ$  ( $T = t_{xx}^2$ ), the interfering term in Eq. (3) will be vanished and the transmission modulation is purely due to the  $s$  dependence of transmission coefficients rather than the interference effect. In addition, if the incident waves are incoherent radiations with random orientations and phases of the electric field, the transmission efficiency described by Eq. (3) will be averaged and degenerated to  $T = (t_{xx}^2 + t_{xy}^2)/2$ . In this case, no polarization interference and efficient modulation can be obtained with the system [the transmission efficiency will be maintained at about 50% with the variation of  $s$ , because of the trade-off between  $t_{xx}$  and  $t_{xy}$ , as shown in Fig. 4(a)].

#### IV. CONCLUSIONS

In summary, a compact and tunable polarization interference system working in the low-frequency region is proposed, employing the artificial planar materials, i.e., two metal screens milled with arrays of rectangular holes. The incident wave can be decomposed into two orthogonal polarization components, which subsequently couple to a single outgoing polarization via near-field coupling. Constructive and destructive polarization interference in the far and near field are suggested, giving rise to an enhancement or suppression of zero-order transmission and hole electric field. Interestingly, the transmission coefficients and phase difference of the two polarization components are dependent on the lateral dislocation of the two screens. Thus, by displacing one metal screen laterally, the polarization interference and transmission efficiency can be modulated efficiently. The experiment confirms that, when the lateral

displacement varies from  $-6$  to  $6$  mm, the transmission intensity decreases almost linearly from 93.1% to 1.4%. It should be mentioned that, by scaling the structural sizes with wavelength, the system and effect may be extended to the THz region. Moreover, the mechanical displacement of the metal screen can be driven by introducing the micro-electromechanical systems [22–24]. The proposed polarization interference system may be employed to construct the microwave or THz switches and modulators.

#### ACKNOWLEDGMENTS

This work is supported by the National Natural Science Foundation of China (Grant No. 12174193) and the Postgraduate Research & Practice Innovation Program of Jiangsu Province (Grant No. KYCX21\_1092).

- [1] A. Yariv and P. Yeh, *Optical Waves in Crystals* (John Wiley & Sons, Canada, 1984).
- [2] Q. Zhou, Intracavity polarization interference filters, *Opt. Commun.* **194**, 11 (2001).
- [3] N. Zhu, Y. T. Wang, J. Liu, J. H. Xie, and H. Zhang, Optical image encryption based on interference of polarized light, *Opt. Express* **17**, 13418 (2009).
- [4] B. Kippelen, Sandalphon, K. Meerholz, and N. Peyghambarian, Birefringence, Pockels, and Kerr effects in photorefractive polymers, *Appl. Phys. Lett.* **68**, 1748 (1996).
- [5] J. Ferre and G. A. Gehring, Linear optical birefringence of magnetic crystals, *Rep. Prog. Phys.* **47**, 513 (1984).
- [6] A. Melikyan, L. Alloatti, A. Muslija, D. Hillerkuss, P. C. Schinler, J. Li, R. Palmer, D. Korn, S. Muehlbrandt, D. Van Thourhout, B. Chen, R. Dinu, M. Sommer, C. Koos, M. Kohl, W. Freude, and J. Leuthold, High-speed plasmonic phase modulators, *Nat. Photonics* **8**, 229 (2014).
- [7] B. X. Li, G. Babakhanova, R. L. Xiao, V. Borshch, S. Siemianowski, S. V. Shiyanovskii, and O. D. Lavrentovich, Microsecond Electro-Optic Switching of Nematic Liquid Crystals with Giant Dielectric Anisotropy, *Phys. Rev. Appl.* **12**, 024005 (2019).
- [8] Y. Uemura, S. Matsuoka, J. Tsutsumi, S. Horiuchi, S. Arai, and T. Hasegawa, Birefringent Field-Modulation Imaging of Transparent Ferroelectrics, *Phys. Rev. Appl.* **14**, 024060 (2020).
- [9] W. H. Wang, H. M. Zhang, B. Li, Z. Li, and Y. P. Miao, Optical fiber magnetic field sensor based on birefringence in liquid core optical waveguide, *Opt. Fiber Technol.* **50**, 114 (2019).
- [10] D. Kim, Y. W. Oh, J. U. Kim, S. Lee, A. Baucour, J. Shin, K. J. Kim, B. G. Park, and M. K. Seo, Extreme anti-reflection enhanced magneto-optic Kerr effect microscopy, *Nat. Commun.* **11**, 5937 (2020).
- [11] N. Jing, C. Yu, K. W. Li, R. Zhang, Z. B. Wang, and C. Wang, Compressive sensing absorption spectroscopy based on photoelastic modulation and single-pixel detection, *IEEE Sens. J.* **21**, 9885 (2021).

- [12] F. Su, B. W. Zhang, and T. H. Li, High speed stress measurement technique based on photoelastic modulator (PEM) and galvano-scanner, *Opt. Lasers Eng.* **136**, 106306 (2021).
- [13] J. M. Hao, Y. Yuan, L. X. Ran, T. Jiang, J. A. Kong, C. T. Chan, and L. Zhou, Manipulating Electromagnetic Wave Polarizations by Anisotropic Metamaterials, *Phys. Rev. Lett.* **99**, 063908 (2007).
- [14] S. Liu, T. J. Cui, Q. Xu, D. Bao, L. L. Du, X. Wan, W. X. Tang, C. M. Ouyang, X. Y. Zhou, H. Yuan, H. F. Ma, W. X. Jiang, J. G. Han, W. L. Zhang, and Q. Cheng, Anisotropic coding metamaterials and their powerful manipulation of differently polarized terahertz waves, *Light Sci. Appl.* **5**, e16076 (2016).
- [15] P. C. Huo, S. Zhang, Y. Z. Liang, Y. Q. Lu, and T. Xu, Hyperbolic metamaterials and metasurfaces: Fundamentals and applications, *Adv. Opt. Mater.* **7**, 1801616 (2019).
- [16] D. M. Liu, T. T. Lv, G. H. Dong, C. Liu, Q. Liu, Z. Zhu, Y. X. Li, C. Y. Guan, and J. Y. Shi, Broadband and wide angle quarter-wave plate based on single-layered anisotropic terahertz metasurface, *Opt. Commun.* **483**, 126629 (2021).
- [17] C. P. Huang, Efficient and broadband polarization conversion with the coupled metasurfaces, *Opt. Express* **23**, 32015 (2015).
- [18] S. T. Xu, F. Fan, M. Chen, Y. Y. Ji, and S. J. Chang, Terahertz polarization mode conversion in compound metasurface, *Appl. Phys. Lett.* **111**, 031107 (2017).
- [19] J. Zi, Q. Xu, Q. Wang, C. Tian, Y. Li, X. Zhang, J. Han, and W. Zhang, Antireflection-assisted all-dielectric terahertz metamaterial polarization converter, *Appl. Phys. Lett.* **113**, 101104 (2018).
- [20] C. P. Huang, Y. L. Wang, and Y. Zhang, Interference-type plasmonic polarizers and generalized law of malus, *J. Opt.* **21**, 105001 (2019).
- [21] C. P. Huang, Y. Zhang, Y. L. Wang, and L. B. Kong, Arbitrarily Directional and Tunable Polarization Rotating Effect with Coupled Metal Screens, *Phys. Rev. Appl.* **10**, 064038 (2018).
- [22] X. G. Zhao, G. W. Duan, A. B. Li, C. X. Chen, and X. Zhang, Integrating microsystems with metamaterials towards metadevices, *Microsyst. Nanoeng.* **5**, 5 (2019).
- [23] Y. H. Chang, J. X. Wei, and C. K. Lee, Metamaterials - from fundamentals and MEMS tuning mechanisms to applications, *Nanophotonics* **9**, 3049 (2020).
- [24] Y. Huang, K. Nakamura, Y. Takida, H. Minamide, K. Hane, and Y. Kanamori, Actively tunable THz filter based on an electromagnetically induced transparency analog hybridized with a MEMS metamaterial, *Sci. Rep.* **10**, 20807 (2020).